Chemical Engineering Journal 485 (2024) 149889

Contents lists available at ScienceDirect

Chemical Engineering Journal

journal homepage: www.elsevier.com/locate/cej

Optimal selection of inversion method for gas-adsorption pore characterization of shales in Wufeng and Longmaxi Formation, Sichuan Basin

Wenbin Jiang [a,b], Mian Lin [a,b,*], Chao Luo [c,d], Zhuo Chen [a,b], Gaohui Cao [a,*], Lili Ji [a,b], Wenchao Dou [a], Kesu Zhong [c,d], Fang Hao [e]

[a] Institute of Mechanics, Chinese Academy of Sciences, Beijing 100190, China
[b] University of Chinese Academy of Sciences, Beijing 100190, China
[c] PetroChina Southwest Oil & Gasfield Company, Chengdu, Sichuan 610051,China
[d] Shale Gas Research Institute of PetroChina Southwest Oil & Gasfield Company, Chengdu, Sichuan 610051, China
[e] School of Geosciences, China University of Petroleum, Qingdao 266580, Shandong, China

ARTICLE INFO

Keywords:
Shale Gas
Low-Temperature Gas Adsorption
Inversion Method
Pore Size Distribution
Large area mosaic SEM imaging

ABSTRACT

The pore space in gas shale spans multiple scales, ranging from nanometers to micrometers with an extremely complex structure and strong microscopic heterogeneity. Existing low-temperature gas adsorption (LTGA) pore size distribution (PSD) analysis models are based on the assumption of a one-dimensional tubular model and there is a lack of sufficient basis for selecting the most appropriate inversion model among the various types available. In this study, a comprehensive characterization of numerous samples from the Wufeng and Longmaxi Formation in the southern Sichuan Basin was conducted using different methods and inversion models. Based on multiple dimensions, such as fitting errors, the correlation between different methods including low-temperature CO2 adsorption (LTCA), nitrogen adsorption (LTNA), and large-scale mosaic Scanning Electron Microscopy (LAM-SEM), the most suitable one-dimensional models for LTCA and LTNA PSD analysis for the studied shale samples are determined. The simulation of gas condensation processes on LAM-SEM images yielded pore volume (PV) in the range of 32–48 nm comparable to the PV characterized by LTNA. Furthermore, the differences observed in PSDs between the gas condensation simulation procedure and the equivalent circular area diameter method indicate that irregular corner regions within larger pores are attributed to the volume of smaller-sized pores during gas adsorption characterization. It is revealed that the correlation between stitched surface area (SA) and maximum methane adsorption is stronger than individual characterizations, indicating that both micropores and mesopores contribute significantly to adsorption, and both characterization methods need to be employed to obtain SSA that influences methane adsorption. The research findings are helpful to the improvement of the multi-scale pore characterization level and evaluation of shale reservoirs.

1. Introduction

Shale gas is of great potential and plays an important part in the natural gas supply. Compared with reservoir rock of conventional oil and gas, the size of dominating pores in gas shales is reduced to the nanometer scale across multiple orders of magnitude, while the porosity is just reduced several times [1–5]. Therefore, the number density of pores in shale is increased significantly. Furthermore, it is disclosed by SEM (Scanning Electron Microscopy) images that pores develop in both organic content and inorganic minerals [6–8]. The organic matter is distributed in a dispersed and blocky form with the size of tens of nanometers to tens of micrometers [9–11]. To obtain a representative PSD of a shale, the field of view needs to be over hundreds of micrometers. Therefore, the scale span from the dominating pore to the representative field of view for shale is more than an order of magnitude larger than that of conventional reservoirs. Existing three-dimensional digital imaging techniques cannot directly meet this requirement, and combining multiple methods to determine the PSD is a more realistic option.

The main methods include low-temperature nitrogen adsorption

* Corresponding authors at: Institute of Mechanics, Chinese Academy of Sciences, Beijing 100190, China (Mian Lin, Gaohui Cao).
E-mail addresses: linmian@imech.ac.cn (M. Lin), caogaohui@imech.ac.cn (G. Cao).

https://doi.org/10.1016/j.cej.2024.149889
Received 26 December 2023; Received in revised form 18 February 2024; Accepted 20 February 2024
Available online 23 February 2024

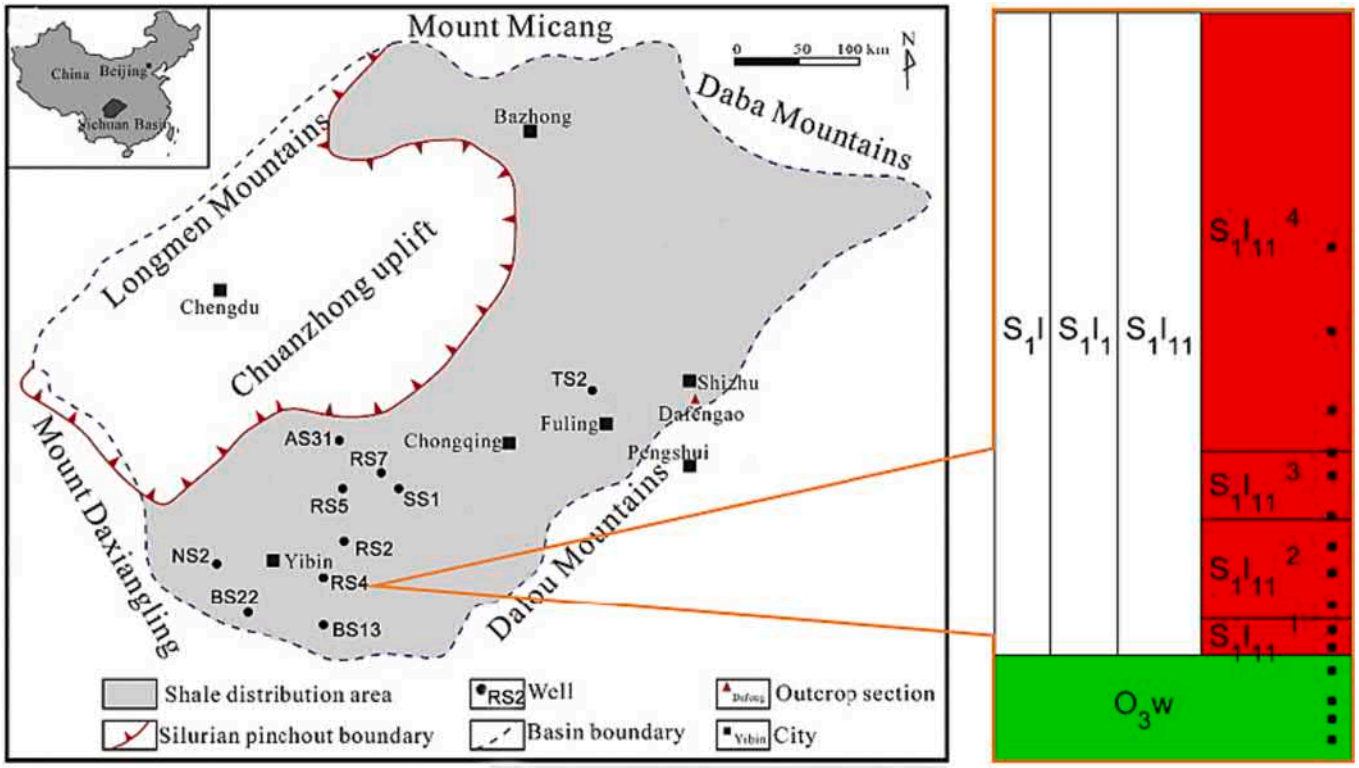

Fig. 1. The location of studied wells and the vertical distribution of the studied samples.

(LTNA), low-temperature carbon dioxide adsorption (LTCA), high-pressure mercury injection (HPMI), large area mosaic SEM image (LAM-SEM), focused-ion-beam SEM (FIB-SEM) and Micro Computed Tomography (μ-CT), etc. [12–15] Low-temperature gas adsorption (LTGA, including LTNA, LTCA, etc.) methods use molecules as probes to detect the pore size, the detectable range spans from the diameter of the molecule to tens of nanometers and hundreds of nanometers. The upper limit depends on the maximum relative pressure (relative pressure which varies from 0 to 1 is the ratio of absolute pressure to the saturated vapor pressure, namely P0, of the gas at the operating temperature) that the apparatus can reach and the inversion model [16]. HPMI interprets the injected mercury volume versus injected pressure to the PV versus size according to the relationship between the size and the capillary force. For a complicated pore network, the obtained PV versus size mainly reflects the volume of the pore body that is controlled by a narrow throat [12,17,18]. Among the imaging methods, only two-dimensional LAM-SEM can representatively cover the mesopores and macropores in the matrix of shale with the highest resolution of 4 nm and the field of view of hundreds of micrometers [1,10].

The understanding of the difference in the characterization using different methods currently still stays at the qualitative stage and the level of basic principle. There is a lack of comprehensive and quantitative comparison. The adoption of the inversion method is relatively arbitrary without a solid foundation, and this may lead to problems of inconsistency and inaccurate. Take the LTNA as an example, as the experimental apparatus is relatively less expensive and the analysis procedure is efficient, this method has been widely used by research institutes and engineering units [19–24]. According to the mechanism that the condensation pressures of gas in pores with different sizes vary, the volume of the respective pores can be measured by the number of condensed molecules. The core of the method is the relationship between the condensation pressure and the pore size. Methods from the BJH (Barrett-Joyner-Halenda) model based on the original Kelvin equation to the modified versions and later the density functional theory (DFT) methods [16,25–27] are developed successively. As the fineness improves, it also leads to variety [28–32]. Considering the differences in the shape of the pore, the content of the pore wall, wall heterogeneity, and stability, tens of DFT-type models have been developed. Inversed PSD with these models varies to different degrees [33]. The common feature of these models is that they all treat the pore space as one-dimensional tubular pores. There is a lack of DFT models that consider multi-dimensional pores. For materials with one-dimensional pore structure, researchers can select the DFT model based on the understanding of the features of the material [34,35]. However, for gas shales with complicated pore structure and strong heterogeneity, the understanding of the optimal DFT model is insufficient and there is a lack of effective guidance and basis for the optimal selection of existing one-dimensional models.

There are four main types of bases for the selection of the LTGA inversion model. The first type is the qualitative similarity in the shape of PSD. Li et al. (2015) utilized BJH and DFT models to interpret the PSD of shale samples and found the results are similar while DFT results show more peaks [36]. Sharifigaliuk et al. utilize the conformance of the trend and peaks of the dV/dlog(W) (the differential PV versus natural log of pore width) curve with incremental pore size as a guideline to qualitatively conclude that the DFT model is better than the BJH and NLDFT models [34]. The second one is the quantitative fitting error between the fitted isotherm and the experimental isotherm. Zhang et al. (2017) showed that the DFT model is more suitable than non-local density functional theory (NLDFT) models as the standard deviation between the DFT-fitted and experimental adsorption isotherms is smallest (<0.5 mmol/g for DFT-fitted, while up to above 2 mmol/g for NLDFT-fitted) [35]. Fu et al. compared the root mean square error (RMSE) of model-fitted isotherms with respect to the experimental ones and found the quenched solid density functional theory (QSDFT) model showed a smaller RMSE than NLDFT models (1.074–2.324 for QSDFT-fitted, while 1.074–2.34 for NLDFT-fitted) [12]. The third one is the quantitative correlation between the derived parameters, such as PV, SA etc. Pang et al. concluded that the DFT model is more suitable than the BJH model as the adjusted R^2 between the DFT-derived SA, PV and average pore

Table 1
The DFT and GCMC kernels concerned in this study.

Adsorbate	DFT / GCMC Kernel	Abbreviation
CO_2	CO_2 at 273 K on carbon (NLDFT model)	CO_2-NLDFT
	CO_2 at 273 K on carbon (MC model)	CO_2-GCMC
N_2	N_2 at 77 K on carbon (slit pore, NLDFT equilibrium model)	N_2-Slit-NLDFT-Equ
	N2 at 77 K on carbon (slit pore, QSDFT equilibrium model)	N_2-Slit-QSDFT-Equ
	N_2 at 77 K on carbon (cylinder. pore, NLDFT equilibrium model)	N_2-Cyli-NLDFT-Equ
	N_2 at 77 K on carbon (cylinder. pore, QSDFT equilibrium model)	N_2-Cyli-QSDFT-Equ
	N_2 at 77 K on carbon (cylinder. pore, QSDFT adsorption branch)	N_2-Cyli-QSDFT-Ads
	N_2 at 77 K on carbon (slit/cylinder. pore, NLDFT equilibrium model)	N_2-Sl/Cy-NLDFT-Equ
	N_2 at 77 K on carbon (slit/cylinder. pores, QSDFT equilibrium model)	N_2-Sl/Cy-QSDFT-Equ
	N_2 at 77 K on carbon (slit/cylinder. pores, QSDFT adsorption branch)	N_2-Sl/Cy-QSDFT-Ads
	N_2 at 77 K on carbon (cylinder./sphere pores, QSDFT adsorption branch)	N_2-Cy/Sp-QSDFT-Ads
	N_2 at 77 K on carbon (slit/cylinder./sphere pores, QSDFT adsorption branch)	N_2-Sl/Cy/Sp-QSDFT-Ads

diameter is higher (0.85 and 0.50 for DFT-derived, while 0.82 and 0.41 for BJH-derived) [37]. Wang et al. investigated the correlations between multifractal parameters using the BJH and DFT models and found the DFT model is optimal [38]. Wei et al. compared the correlation of SA and PV using different models and found that the consistency of micro-pores using different models is higher than that of *meso*-pores [39]. The last one is the conformance with the inversed PSD from other LTGA isotherms. Wang et al. used the micro-PSD obtained by GCMC (Grand Canonical Monte Carlo) and NLDFT models applied on the LTCA isotherms of 5 shale samples to evaluate other models applied on the LTNA isotherms. It is found that the HK (Horvathe-Kawazoe) model results showed a similar trend as the CO_2-GCMC results, while the NLDFT and QSDFT results show different trends [33]. Existing studies showed that the inversed PSD by different models and from different LTGAs can vary significantly. The optimal models obtained from different studies are inconsistent. The root cause lies in the complex pore structure of shale, which affects the feasibility of using simplified one-dimensional models. In general, it is believed that DFT-type models are superior to the BJH model. However, the DFT model has multiple variants and there is a lack of further and comprehensive evaluation of their differences. For the Wufeng and Longmaxi formation shale in the Sichuan Basin, there is a wide variety of developed pore types, and research on how to determine the widely applicable and most suitable PSD is rare.

On the other hand, with the development of imaging methods, obtaining large-scale high-resolution images has become possible, providing new means for further validating the optimal model of LTGA. However, there is a lack of effective research on the correlation between the PSD characterized by imaging and the PSD characterized by LTNA. This study aims to optimize the inversion models by simultaneously employing different approaches such as LTCA, LTNA, and LAM-SEM for characterization. The optimization will be based on various aspects, including the fitting errors of each model and the correlation of the overlapping portions characterized by different models. This paper is arranged as follows: the samples and methods investigated in this study are introduced in Section 2, and the optimization procedures and results will be provided in Section 3, finally, the conclusions are drawn.

2. Samples and methods

2.1. Sample information

The 106 shale samples investigated in this study were collected from 10 shale gas wells located in the southern region of the Sichuan Basin, China (as shown in Fig. 1). These wells include AS31, BS22, NS2, RS7, RS2, RS4, RS5, TS2, BS13 and SS1H, belonging to the Changning, Weiyuan, Luzhou, and Yuxi blocks of PetroChina. The samples belong to the Wufeng Formation and the 1st to 4th sublayers of the 1st submember of the first Member of Longmaxi Formation. The depths of the samples range from 1500 m to 4400 m. 6–18 samples are obtained from each well. Fig. 1 illustrates the vertical distribution of samples from the RS4 well. The TOC and mineral contents of the analyzed samples can be further examined in the published work [40].

2.2. Low temperature CO_2 adsorption and N_2 adsorption

2.2.1. Experimental procedure

The studied samples are crushed and sieved to obtain 1–3 g particles with a size range of 20–40 mesh [29]. Before loading into the specific surface area and pore size analyzer (Beishide 3H2000-PS1, produced by Beishide Instrument, Beijing, China) for adsorption procedures, the particles were vacuumed and degassed at 105 °C for at least 4 h [41–43]. LTCA tests were conducted at 0 °C with a relative pressure range of 0–0.033. LTNA tests were performed at 77.3 K with a relative pressure range of 0–0.99.

2.2.2. Inversion models of PSD

Previous studies have shown that the desorption branches of LTNA isotherms mainly reflected the controlling effect of pore throat on the pore body and cannot characterize the size of the pore space accurately [44]. Therefore, the adsorption branches of LTNA isotherms are utilized to interpret PSD [45]. Previous studies have shown that DFT-type models are more effective in characterizing micropores compared to BJH or DH models [18,34]. Therefore, only DFT models are considered in this study. The obtained LTCA isotherms and LTNA isotherms were imported into Quantachrome's ASiQwin software. Various built-in models, including multiple NLDFT, QSDFT, and GCMC models, were used to generate PSD results. The models and their corresponding abbreviations used in this study are listed in Table 1.

For LTCA, both NLDFT and GCMC models considering the slit-shape-type pore were employed. For LTNA, there are 10 inversion models belonging to the NLDFT and QSDFT categories. Within each category, different models vary in pore geometry and condensation and evaporation mechanisms. The pore geometries include slit, cylinder, sphere, and their combinations. The condensation and evaporation mechanisms include the adsorption branch and equilibrium transition. These two mechanisms describe the gas condensation and evaporation processes in one-dimensional pores, which may not be the same in complex porous networks. Therefore, both kinds of models are applied to interpret the adsorption branch and the best one is determined through comprehensive analysis.

Both the NLDFT and QSDFT categories include the silt pore with equilibrium transition model, the cylindrical pore, and the combination of slit and cylindrical pores with equilibrium transition models. Only the QSDFT category has the cylindrical pore, the combination of slit and cylindrical pores, the combination of cylindrical and spherical pores, and the combination of slit, cylindrical and spherical pore with adsorption branch models. Theoretically, a more diverse range of inversion models can be generated with different combinations of pore types and based on the consideration of surface heterogeneity. However, for gas-bearing shale with complex pore structure, it is necessary to establish an appropriate equivalent model. There is a lack of effective guidance in this regard. This study aims to evaluate the above 12 models and select the ones that can most reasonably characterize the pore structure of the studied shale samples, in order to provide a foundational understanding for the development of more refined equivalent models in the future.

When performing PSD analysis using NLDFT/QSDFT/GCMC, a fitting error is provided as an evaluation metric to assess the degree of fit

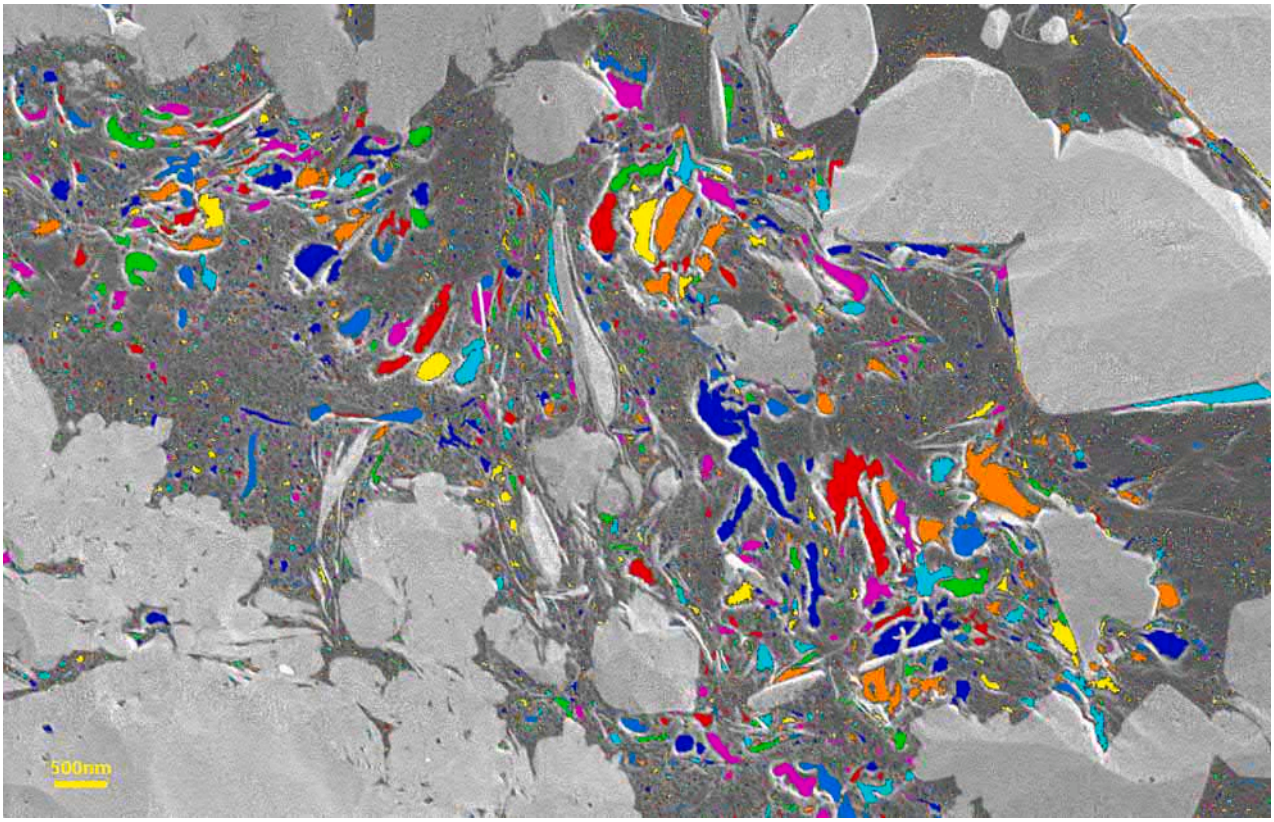

Fig. 2. An example of separating the void pixels based on connectivity.

to the experimental isotherm which has the following expression.

$$\delta = \frac{\sum_{i=1}^{N} \frac{\left|V_{fit,i} - V_{measure,i}\right|}{V_{measure,i}}}{N} \times 100\% \quad (1)$$

where δ is the fitting error, N is the number of data points in the experimental isotherm. $V_{measure,i}$ is the gas adsorption amount at the ith relative pressure point, while $V_{fit,i}$ is the fitted one.

2.3. Large area mosaic SEM imaging

In recent years, with the advancement of technology, LAM-SEM imaging of shale has become increasingly mature. This technique enables two-dimensional imaging with a resolution of 4 nm and a range of hundreds of micrometers. By observing grayscale differences, it is possible to distinguish pores and obtain their distribution and morphological features in two-dimensional space Compared to traditional single-field SEM imaging, the observation range has been significantly expanded, reaching dimensions of hundreds of micrometers in a single dimension, which is close to the size of particles used for gas adsorption, resulting in more representative results.

The samples are first mechanically cut into 1 cm-sized cubes, followed by mechanical polishing and argon ion polishing of the cubes' vertical bedding planes to obtain a smooth surface. The samples undergo large-scale scanning using multiple-patch stitching on the Zeiss Merlin field emission scanning electron microscope (FE-SEM), employing ATLAS 5 software. Initially, a consolidation scan is performed at a resolution of 1 μm/pixel, followed by the selection of representative areas for high-precision, large-field scanning with a resolution of 4 nm/pixel and a range of 400 μm × 400 μm. The sample preparation and imaging procedure mentioned above were conducted at the Institute of Geology and Geophysics, Chinese Academy of Sciences. More details on the LAM-SEM imaging can be referred to Wu et al. (2020) [1]. Appendix 1 includes the results of representative analysis, and previous studies have obtained representative sizes around 150 μm using different methods [46].

The resulting images are stored as nearly ten thousand pictures with dimensions of 1024 × 1024 pixels. There is a situation where a large number of pores are divided into serval parts in different images, which may lead to the subdivision of the same pore space. To avoid this issue, we stitched adjacent sets of 14 × 14 images to create large images with dimensions of at least 14336 × 14336 pixels, resulting in around 50 images in total. This approach significantly reduces the occurrence of "subdivided pore space" for the same pore. The analysis of pore area versus pore diameter was performed individually on each large image, and the pore areas in different size ranges were ultimately summarized.

The commonly used method for analyzing pore area-pore size is based on the grayscale difference between pores and matrix. By setting a reasonable threshold, the image is segmented into a binary image, and the connected regions with pore pixel values in the binary image are used to calculate their areas. The diameter of a circle with an equivalent area is considered the diameter of the connected region. This method is based on the two-dimensional connectivity of pores, making it easy to operate and intuitive, and it is widely used. It is referred to the "EqDia" (equivalent diameter) method in this study. Fig. 2 illustrates an example where different connected regions are represented by different colors (due to a large number of connected regions, there may be instances where the same color is used in multiple regions).

In addition, we propose a novel analysis method. This method is based on the principle that the condensation pressure varies in different pore sizes during LTGA, and the condensation process is not limited by connectivity. Therefore, it can be assumed that all pores in the two-dimensional image are connected in the three-dimensional space, eliminating the need for additional connectivity determination. By simulating the LTGA process with increasing relative pressures, gas condensation occurs in pore spaces of different sizes. This corresponds to

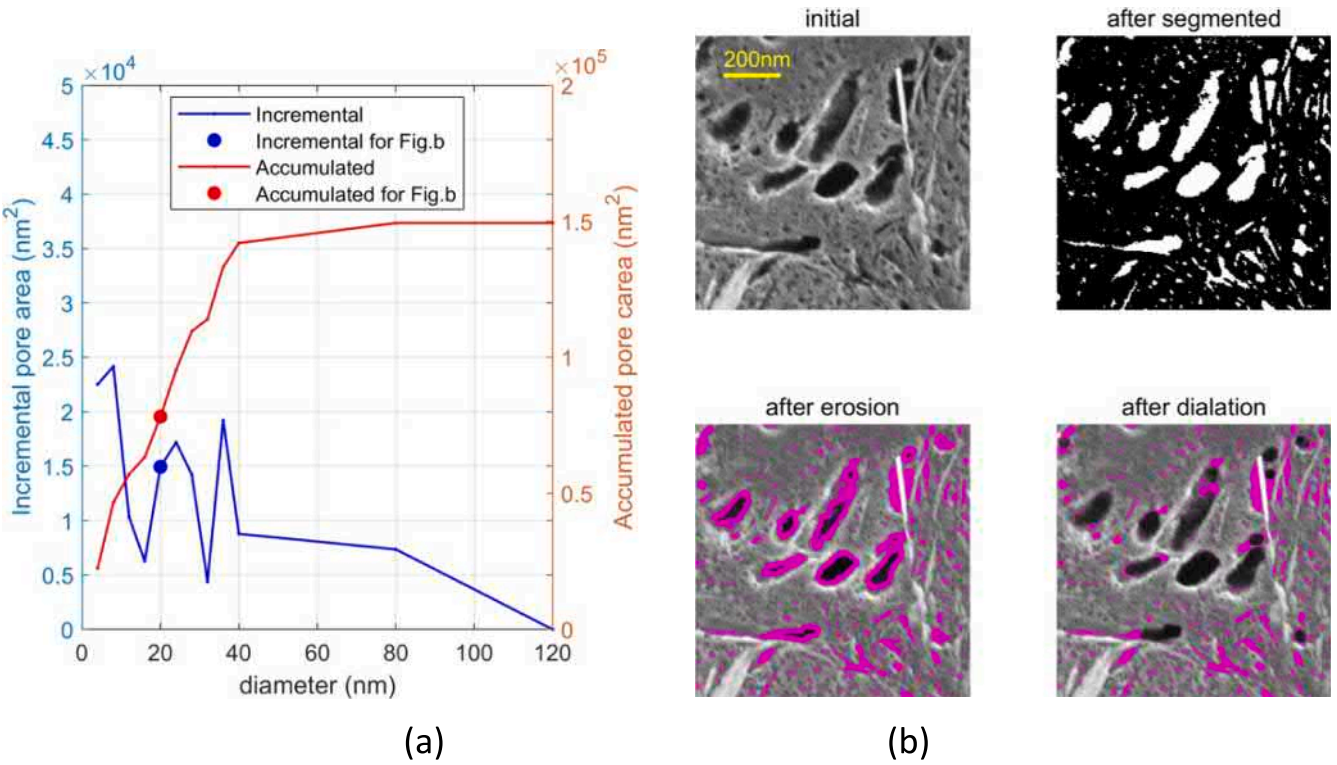

Fig. 3. Analysis result (a) and schematic diagram of condensation region identification process (b).

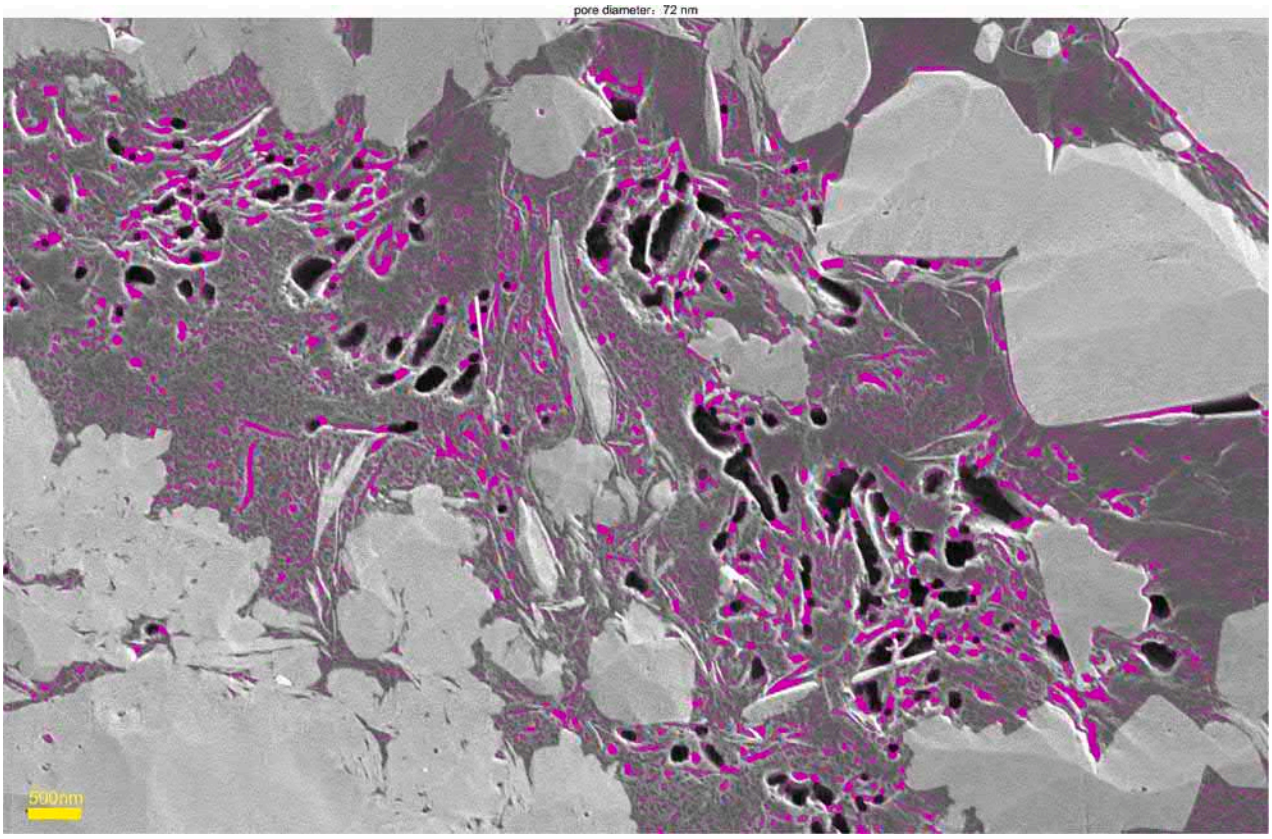

Fig. 4. Regions undergoing "condensation" for the image shown in Fig. 2.

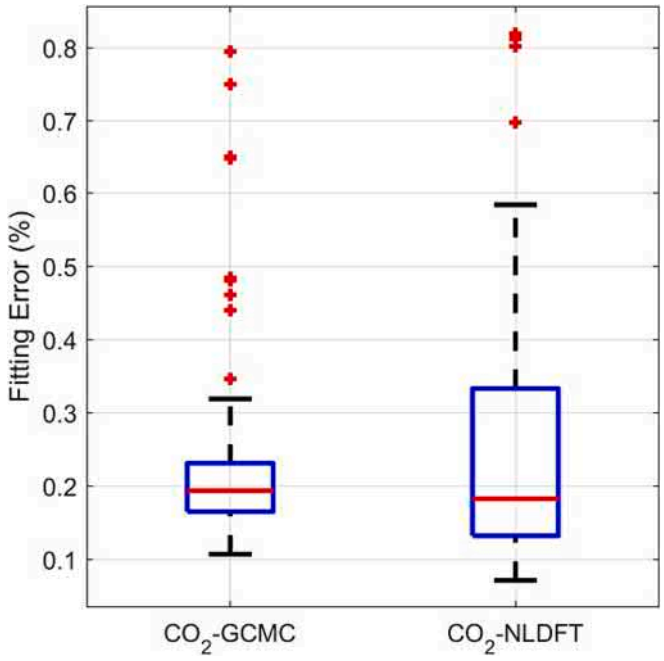

Fig. 5. Distribution of fitting errors for 106 shale samples using different LTCA inversion models.

determining the portion of connected regions with curvature radii smaller than the corresponding values in all connected regions. The areas of these regions are then aggregated to obtain the cumulative pore area from the minimum pore size to the given pore size. The differential pore area corresponding to the specific pore size can be determined. This method is referred to "CondSim" (Condensation Simulation) method here.

The specific process is achieved using two morphological image operations: erosion and dilation. Pore pixels are labeled as 1. In the erosion process, for each pore radius r, a circular structuring element matrix is constructed with the corresponding radius (the circular region with a radius of r in the center is assigned a value of 1, while the rest are assigned 0, it can also be referred to as a convolution kernel). Each pixel in the image is processed, and if both the surrounding pixels within the convolution kernel are pores, the pixel remains a pore; otherwise, it is labeled as a matrix. Through the erosion process mentioned above, the region from the pore wall to the interior with a radius of r can be identified and labeled as matrix pixels. Furthermore, the dilation operation is applied to the eroded image using the same convolution kernel. If any pore is present in the surrounding pixels within the convolution kernel region, the pixel is considered a pore; otherwise, it is a matrix. By performing erosion and dilation operations, the regions with a diameter of the meniscus smaller than 2*r can be identified as the areas where "condensation" occurs. The specific process is illustrated in Fig. 3.

Fig. 4 illustrates the regions undergoing "condensation" (highlighted in pink) performing the aforementioned method on the image shown in Fig. 2.

By simulating the LTGA and condensation process with morphology operations on a LAM-SEM image with a resolution of 4 nm and a FOV of 400 μm, we can obtain the pore area-size distribution, $S_{SEM}(d)$, ranging from 4 nm to the micrometer scale. $S_{SEM}(d)$ represents the cumulative pore area using pores ranging from the smallest size to a diameter of d, and the unit is nm^2. Assuming that the pore size remains constant in the direction perpendicular to the SEM image with a thickness of 1 nm, we can calculate the pore volume-size distribution $V_{SEM}(d)$. $V_{SEM}(d)$ represents the cumulative PV using pores ranging from the smallest size to a diameter of d, and the unit is cm^3/g. These two distributions are related by the following equation:

$$V_{SEM}(d) = \frac{S_{SEM}(d) \times 10^{-14} \times 10^{-7}}{S_{SEM,total} \times 10^{-8} \times 10^{-7} \times \rho_{bulk}} = \frac{S_{SEM}(d)}{S_{SEM,total} \times 10^{6} \times \rho_{bulk}} \quad (2)$$

where $S_{SEM,total}$ is total area of LAM-SEM images, the unit is μm2, ρ_{bulk} is the bulk density of the shale sample, and the unit is g/cm^3. Besides the morphology operation (CondSim) method, the pore area-size distribution obtained by the EqDia method can also be transformed into the pore volume-size distribution according to Eq. (2).

2.4. High-pressure isothermal methane adsorption

The methane adsorption capacity in shale gas is a key parameter for evaluating gas content. The micro-pore surfaces in shale provide sites for methane adsorption, and the methane adsorption characteristics of samples are closely related to the micro-pore structure [47]. Therefore, in addition to the correlation analysis between different pore structure characterization methods, this study further investigates the correlation between high-pressure methane adsorption characteristics and the results of different gas characterizations to clarify the pore range that contributes primarily to methane adsorption.

The sample is ground and approximately 100 g of particles in the size range of 8–20 mesh (with diameters ranging from 0.84 nm to 2.36 nm) are selected for high pressure methane adsorption experiment. The samples were dried and vacuumed at 105 °C for at least 7 h. Subsequently, the sample will be loaded into a volumetric high-pressure gas adsorption instrument (3H2000-PH690) developed jointly by the Institute of Mechanics, Chinese Academy of Sciences, and Beishide Instrument. The methane adsorption isotherms are measured with 12 pressure points spanning 0.5–50 MPa at a constant temperature of 40 °C. The detailed calculation procedure for the adsorption amount can be referred to Jiang et al. (2022) [40]. The measured adsorption isotherms will be fitted using the three-parameter Langmuir equation with the following form.

$$V_{ex}(p) = \left(\frac{V_L p}{p_L + p}\right)\left(1 - \frac{\rho_{free}}{\rho_{ads}}\right) \quad (3)$$

where $V_{ex}(P)$ represents the measured excess adsorption amount (ml/g), V_L is the maximum adsorption capacity (ml/g), P_L is the Langmuir pressure (MPa), ρ_{ads} is the adsorbed phase density (g/cm^3), and ρ_{free} is the density of free state methane (g/cm^3) at pressure P (MPa).

3. Results and discussions

3.1. Comparison of fitting errors of different methods

When performing PSD analysis using NLDFT/QSDFT/GCMC, a fitting error is provided as an evaluation metric to assess the degree of fit to the experimental isotherm which has the following expression.

When conducting PSD analysis using NLDFT/QSDFT/GCMC, the fitting error generated by the inversion models serves as an evaluation metric for assessing the quality of the model fit. Firstly, the LTCA isotherms and LTNA isotherms are individually analyzed using various inversion models listed in Table 1. Subsequently, a comparative analysis of the fitting errors is performed to assess the quality of the fits across the different models.

3.1.1. Inversion models for LTCA isotherms

The distribution of fitting errors of the 106 studied samples between the optimal fit of the adsorption isotherms obtained from CO_2-GCMC and CO_2-NLDFT models and the experimental isotherms are illustrated with a boxplot in Fig. 5. The red line represents the median value of the fitting error, while the blue box indicates the interquartile range (25th to 75th percentile). The black dashed line represents the range of non-outlier values, and the red dots represent any outliers. It can be observed that the median values of the fitting errors for both models are

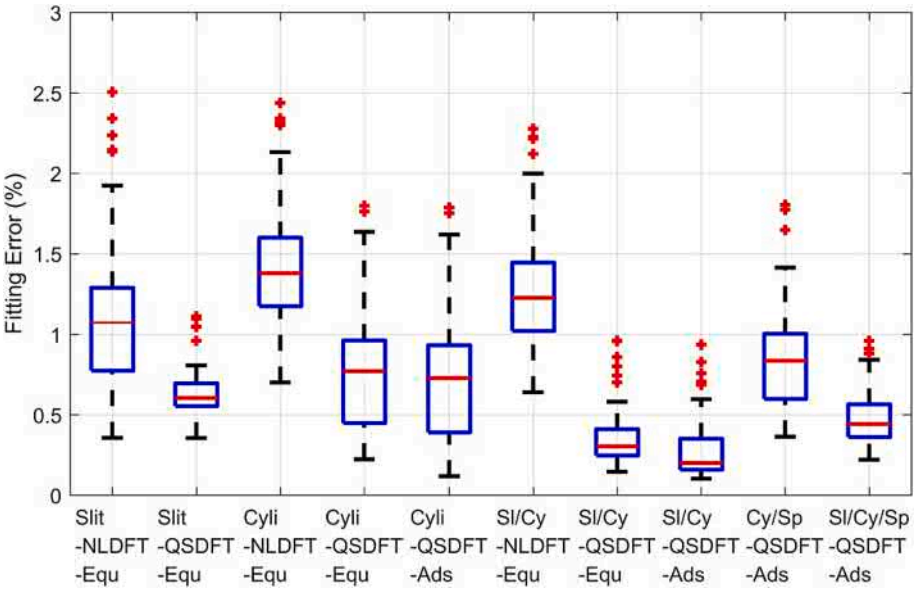

Fig. 6. Distribution of fitting errors for 106 shale samples using different LTNA inversion models.

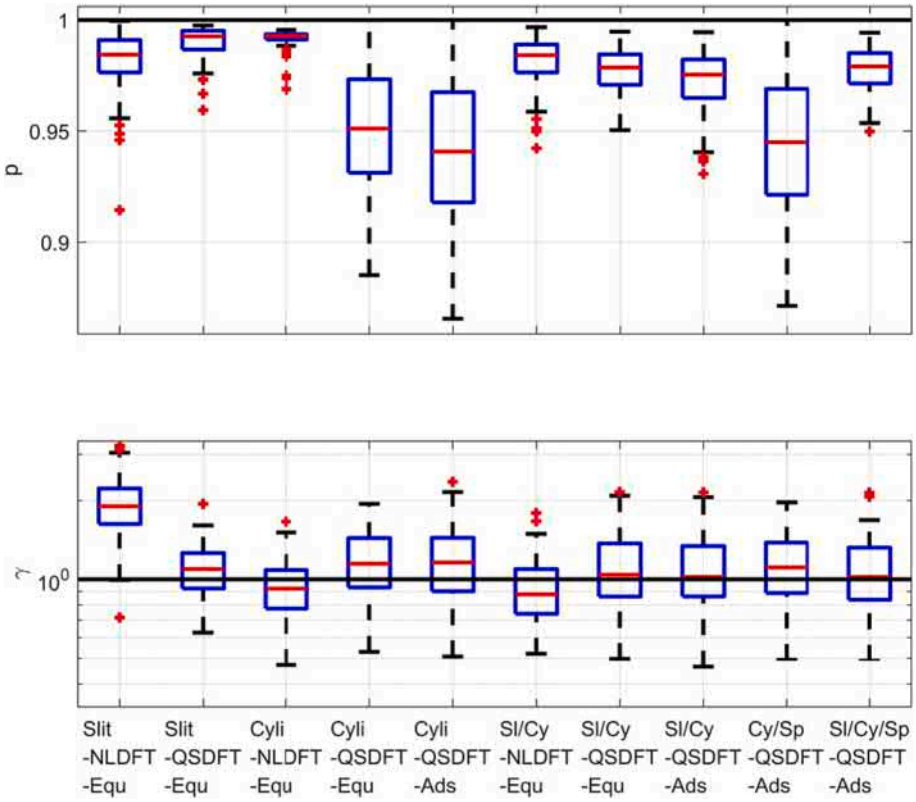

Fig. 7. Distribution of p and γ for 106 shale samples using the CO_2-GCMC model and different LTNA inversion models.

relatively close, with CO_2-NLDFT showing slightly lower values. However, the interquartile range and the range of non-outlier values for the CO_2-NLDFT model are broader compared to the CO_2-GCMC model. Therefore, further comprehensive assessments are required to make a preferable selection between the two models.

Chandra also compared these two methods from the perspective of fitting error and analyzed seven samples. It was found that in most cases, GCMC exhibited smaller errors [48]. In contrast to the CO2-NLDFT model based on a one-center Lennard-Jones potential, CO2-GCMC is based on a three-center potential function, capable of incorporating both Lennard-Jones potential and electrostatic contributions [49]. Pang et al. also conducted a comparison of the fitting errors between CO_2-GCMC and CO_2-NLDFT methods. The study found that the CO_2-GCMC method exhibited relatively smaller fitting errors compared to the CO_2-NLDFT method [37].

3.1.2. *Inversion models for LTNA isotherms*

The distribution of fitting errors between the optimal fit of the

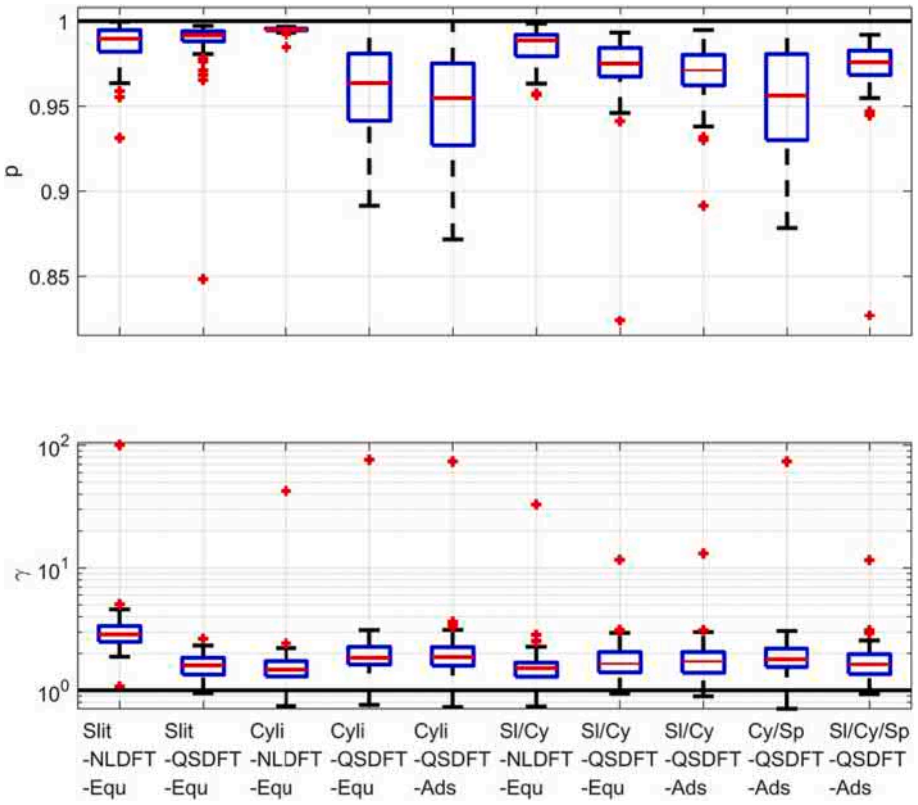

Fig. 8. Distribution of p and γ for 106 shale samples using the CO_2-NLDFT model and different LTNA inversion models.

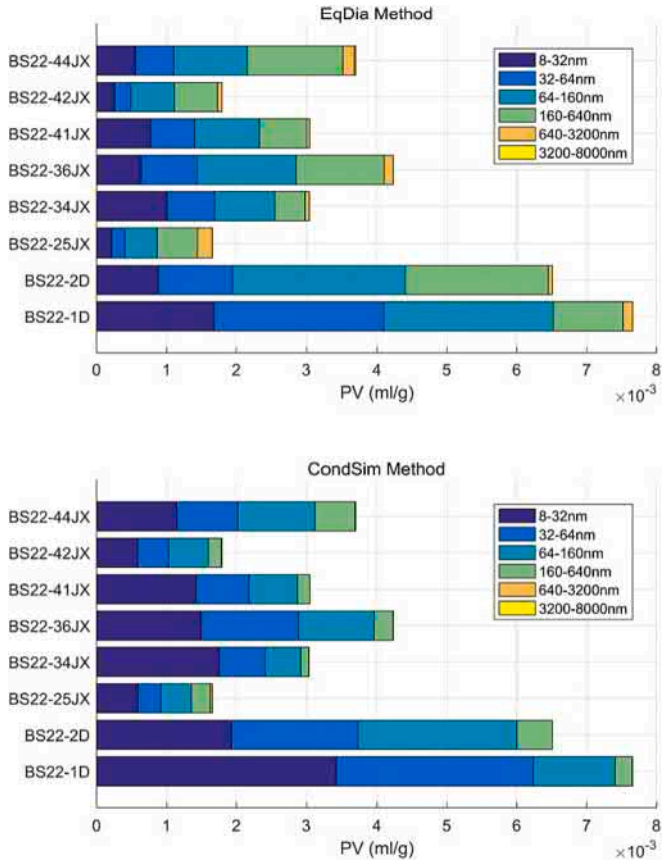

Fig. 9. Pore volume-size distributions of 8 BS22-well samples from LAM-SEM using two methods.

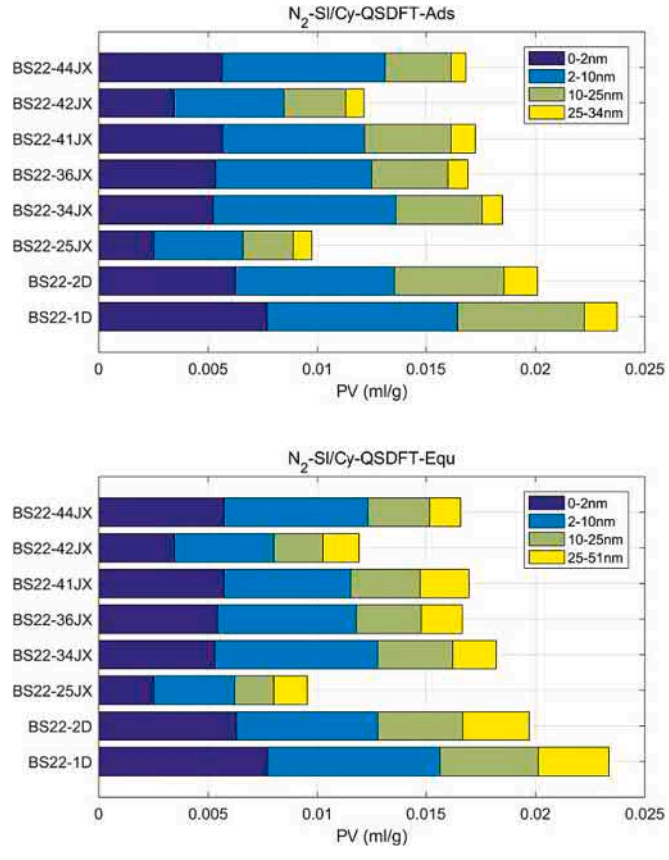

Fig.10. Pore volume-size distributions of 8 BS22-well samples from LTNA using two methods.

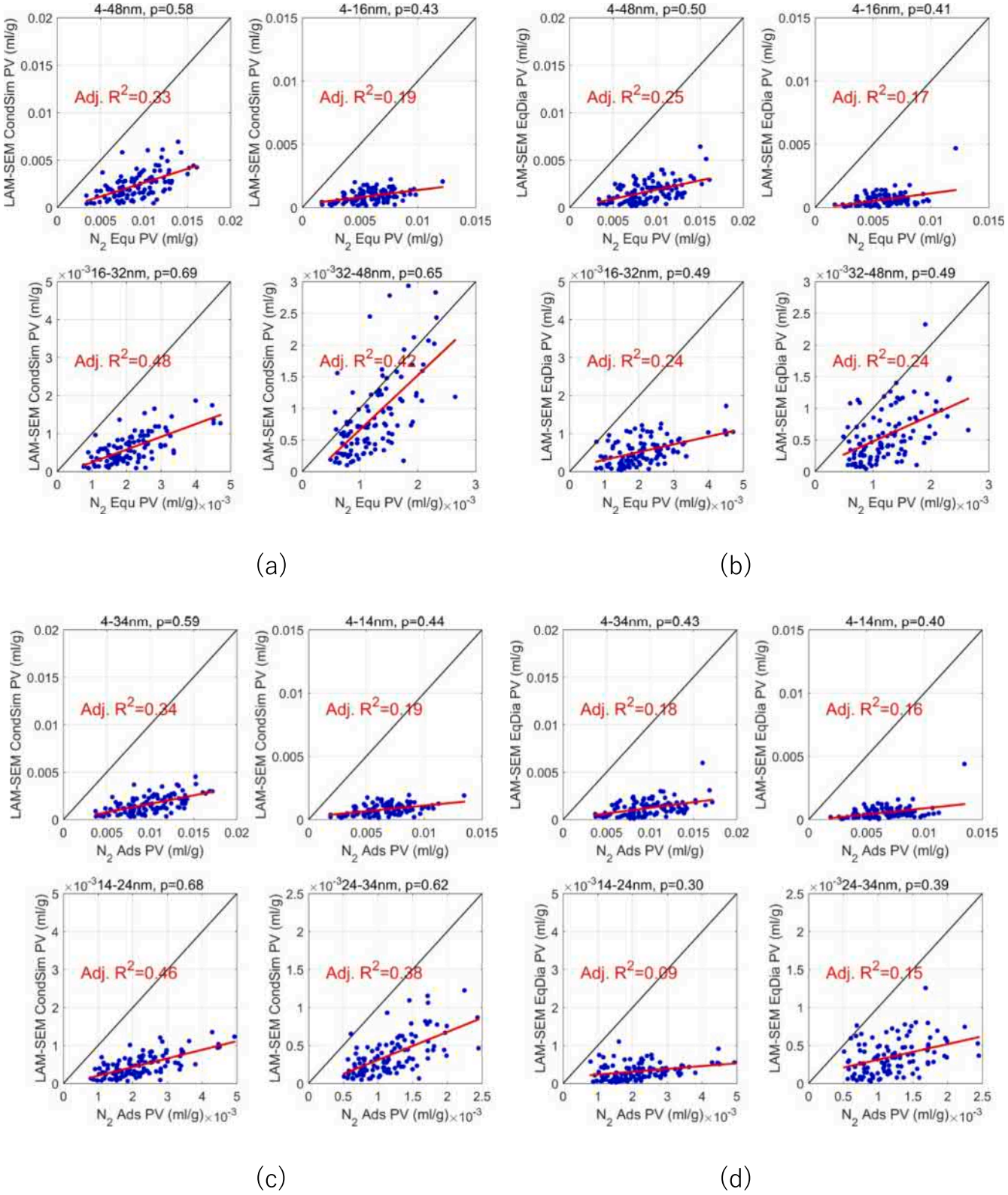

Fig. 11. Correlation between PV obtained by LAM-SEM and LTNA for 106 shale samples. CondSim versus QSDFT-Sl/Cy- Equ (a), EqDia versus QSDFT-Sl/Cy- Equ (b), CondSim versus QSDFT-Sl/Cy- Ads (c), EqDia versus QSDFT-Sl/Cy- Ads (d),

adsorption isotherms obtained from 10 different NLDFT/QSDFT models and the experimentally measured adsorption isotherms for the 106 samples are illustrated with a boxplot in Fig. 6. From the median relative fitting errors, it can be observed that three NLDFT models are significantly higher than the other QSDFT models, indicating that the QSDFT models, which consider surface heterogeneous, can better characterize the LTGA characteristics of shale samples. Among all the QSDFT models, both the N_2-Sl/Cy-QSDFT-Equ model, which considers equilibrium transition, and the N_2-Sl/Cy-QSDFT-Ads model, which employs an adsorption branch, exhibit significantly lower median relative errors

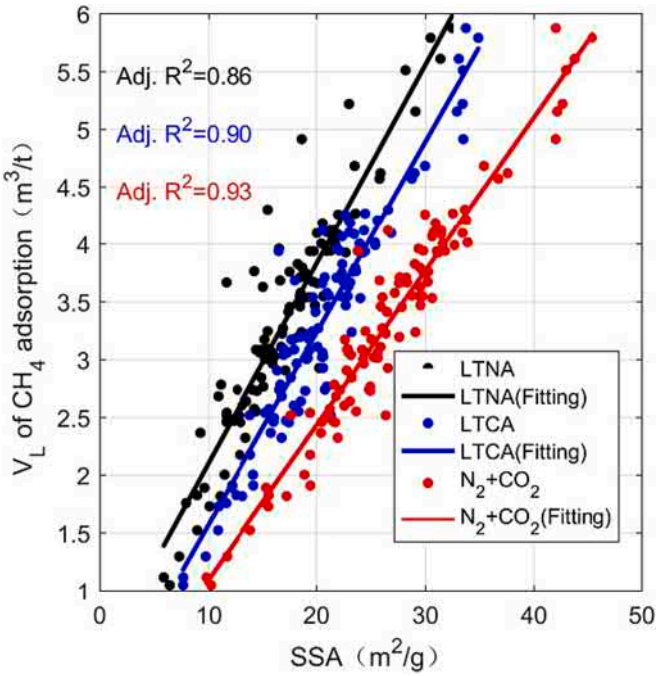

Fig. 12. Correlation analysis between V_L and SSAs determined by different methods.

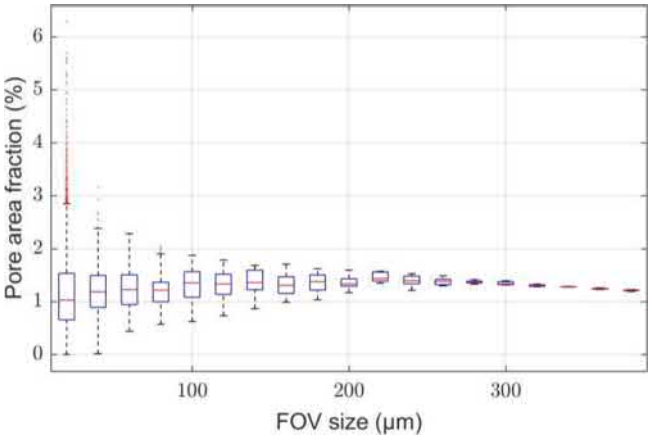

Fig. A1. Variation of pore area fraction with the width of the analyzed domain.

compared to the other models. Additionally, the 25th to 75th percentile range of these two models is closer to the zero-axis compared to the other QSDFT models. This suggests that among the five pore types considered, namely slit-shaped, cylindrical, slit-shaped + cylindrical, cylindrical + spherical, and slit-shaped + cylindrical + spherical, the model incorporating a combination of slit-shaped and cylindrical pores best matches the LTGA isotherm characteristics of shale samples. In this model, pores with diameters below 2 nm are considered slit-shaped pores, while those above 2 nm are considered cylindrical pores.

Within the two models, it is observed that the model utilizing the adsorption branch, which is utilized by Chandra et al. to calculate the PSD [48], exhibits slightly lower median relative errors. However, the 25th to 75th percentile range and the range of non-outlier values for this model are slightly wider compared to the model considering equilibrium transition. Further comprehensive assessments are required to make a preferable selection between these two models.

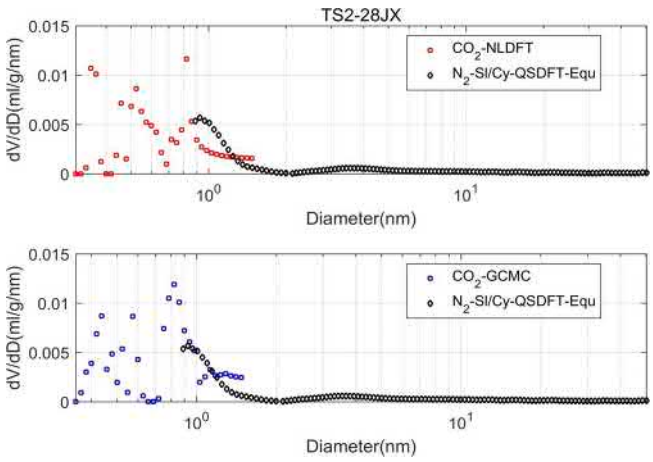

Fig. A2. PSDs derived with different model for the TS2-28JX sample.

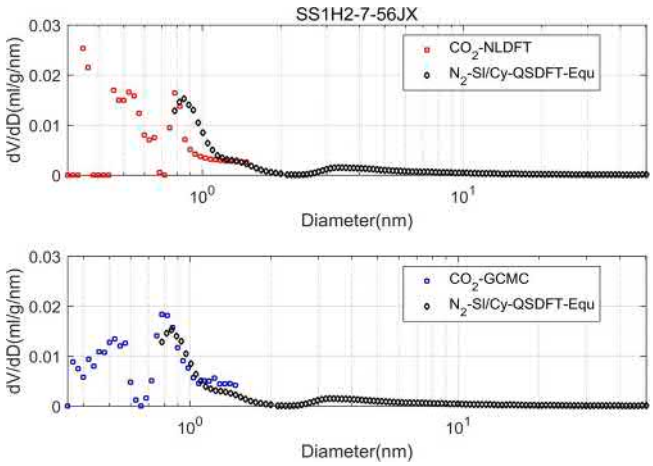

Fig. A3. PSDs derived with different model for the SS1H2-7-56JX sample.

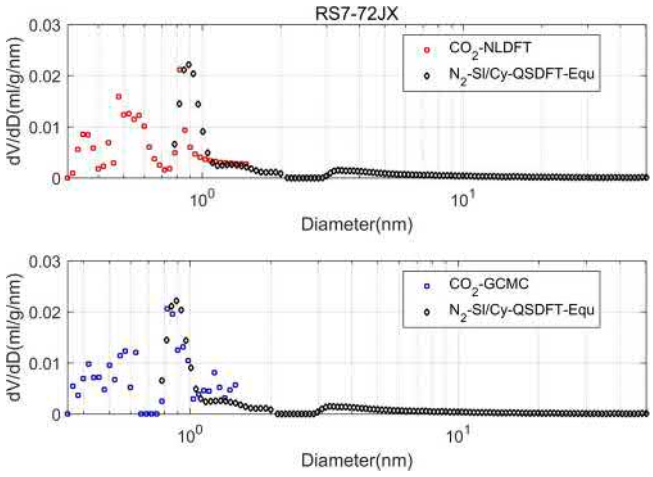

Fig. A4. PSDs derived with different model for the RS7-72JX sample.

3.2. Correlation analysis of the overlapped between PSD from different LTGA methods

The maximum pore diameter $d_{CO_2,\max}$ obtained from the analysis of LTCA using GCMC and NLDFT models is 1.4748 nm, while the minimum pore diameter $d_{N_2,\min}$ obtained from the analysis of LTNA using different

NLDFT/QSDFT models is 0.6140 nm. The existence of overlapping PSDs obtained from these two different characterization methods provides an opportunity to assess their correlation. Let $V(d)$ denote the cumulative PV in cm^3/g from the smallest pore to a pore diameter of d. Thus, $V_{CO_2}(d)$ and $V_{N_2}(d)$ denote the PV distributions obtained from LTCA and LTNA, respectively. Two parameters are defined for correlation analysis: the Pearson correlation coefficient p [50] of $V_{CO_2}(d)$ and $V_{N_2}(d)$ in the range of $d_{N_2,\min}$ to $d_{CO_2,\max}$, and the ratio γ of the PV characterization of N_2 adsorption to CO_2 adsorption.

$$\gamma = \frac{V_{N_2}(d_{CO_2,\max}) - V_{N_2}(d_{N_2,\min})}{V_{CO_2}(d_{CO_2,\max}) - V_{CO_2}(d_{N_2,\min})} \tag{4}$$

For the 106 samples, cross-calculations of p and γ values between two LTCA inversion models and 10 LTNA inversion models were performed.

Firstly, the comparison between the CO_2-GCMC model and the different LTNA inversion models is analyzed. As shown in Fig. 7, the Pearson correlation coefficients p for all models are greater than 0.9, except for the QSDFT-Equ/Ads model for cylindrical pores and the QSDFT-Ads model for the combination of cylindrical and spherical pores. The median p-values for the other models are all greater than 0.95, indicating a strong correlation between the PSDs obtained from the two gas adsorption methods. Interestingly, the NLDFT model for cylindrical pores, which had relatively larger fitting errors in the previous analysis, actually shows the median p-value closest to 1. This suggests that, in situations where the correlation coefficients are generally high, the Pearson correlation coefficient may not be sensitive enough to reveal subtle differences.

Looking at the PV ratio γ, except for the NLDFT model for slit-shaped pores, which has a significantly larger median value than 1, the median values for the other models are generally close to 1. This indicates that the PVs within the overlapping pore size range characterized by low-temperature CO_2 and N_2 adsorption are relatively close.

Next, the comparison between the CO_2-NLDFT model and the different LTNA inversion models is examined. As shown in Fig. 8, similar to the CO_2-GCMC model, the Pearson correlation coefficients are generally high, with median values closer to 1. However, the distribution of outliers is wider, and the distribution appears more scattered. Regarding the PV ratio γ, the median values for all models are significantly greater than 1. This indicates that the PVs within the 0.6140 nm to 1.4748 nm range obtained from the NLDFT analysis of LTCA are noticeably smaller than the overlapping pore size range characterized by N_2 adsorption.

In summary, it is observed that the PVs within the overlapping range calculated by the CO_2-GCMC model are closer to those obtained from N_2 adsorption. For the PSDs, as shown in the appendix, the width of the peaks around 0.8 nm founded in PSD derived by CO2-GCMC and N2-Sl/Cy-QSDFT-Equ model are more consistent. Therefore, it is more inclined to recommend using the CO_2-GCMC method for PSD analysis of shale samples from the Wufeng and Longmaxi Formation in the Sichuan Basin, China. This conclusion aligns with the findings reported by Pang et al. [37], although they used the correlation between SA and PV obtained from the two models to determine the best model. The CO_2-GCMC model has also been used by Wang et al. [33] to evaluate inversion models for LTNA isotherm.

In the comparison of LTNA inversion models, particularly for the combination of slit-shaped and cylindrical pores with equilibrium transition (Equ) and adsorption branch (Ads) models, it remains challenging to clearly determine the superiority through the correlation analysis between CO_2 and N_2 adsorption.

3.3. Correlation analysis of PSDs obtained by LTNA and LAM-SEM images

By using high-resolution SEM imaging, PSDs as low as 4 nm in diameter can be obtained, which overlaps with the characterization range of LTNA (up to 50 nm). A comparison can be made between the PSDs characterized by both methods in the overlapping range. However, there is currently limited research in this area. To establish a correlation between these two kinds of methods, there are challenges in terms of sample heterogeneity, dimensional characterization, and analytical principles. The current realistic approach is to analyze a large number of samples to select the overall optimal model among existing ones. In this study, 106 shale samples from different formations and wells in the southern Sichuan Basin are selected for analysis. The PSDs obtained by performing different analysis methods on LAM-SEM images and QSDFT-Sl/Cy-Equ (referred to Equ below for convenience) and QSDFT-Sl/Cy-Ads (referred to Ads below for convenience) inversion models on LTNA isotherms were compared.

For LAM-SEM images, both the EqDia method and CondSim method were used to calculate PSDs. Taking 8 shale samples from the BS22 well as an example to demonstrate the difference of results obtained by these two methods. As shown in Fig. 9, the pore volume-size distribution is presented using stacked bars with different colors indicating different pore size ranges. It can be observed that the proportion of larger PVs determined by the EqDia method is higher than that obtained from the CondSim method. The reason behind this difference lies in the fact that in the macroscopic pores, particularly in localized regions such as the edge or regions with smaller liquid curvature, condensation occurs at lower relative pressures (compared to the relative pressure at which gas condensation occurs in the central part of the macroscopic pores) during the condensation process. Consequently, this portion of the volume is accounted for in smaller-sized pores. The volume of a connected region can be divided into several parts according to the sequence of gas condensation in the CondSim method.

For the LTNA isotherms, the two preliminary selected models, Equ and Ads models, were applied to interpret PSDs. The same 8 shale samples from the BS22 well were taken as an example to demonstrate the difference, as shown in Fig. 10. The stacked bars in different colors represent the PV in different pore size ranges. It can be observed that the total PVs obtained are consistent for the same sample since both methods are based on the same adsorption isotherm. However, the PSDs obtained by the two models differ. The Ads model reveals a PSD ranging from 0 to 34 nm. In contrast, the Equ model shows a PSD ranging from 0 to 51 nm, with a higher proportion of larger PVs compared to the former model.

The underlying reason for this discrepancy lies in the difference in the gas condensation/evaporation mechanisms described by these two models. For a one-dimensional pore structure, the nitrogen gas condenses through liquid bridging and exhibits a certain degree of hysteresis, while evaporating through the gas–liquid two-phase meniscus. For pores of the same size, the condensed liquid bridge forms at a higher relative pressure compared to the relative pressure at which gas evaporates [51]. The pore size interpreted by the adsorption branch model is smaller compared to that interpreted by the equilibrium transition model for the same relative pressure.

Based on the above analysis, we have four sets of results: two from LAM-SEM and two from the interpretation of LTNA isotherms. A cross-comparison of these results can be performed. For each comparison, the correlation between the PVs characterized by the two methods within the overlapping pore size range is examined, both overall and within different sub-intervals. The results are shown in Fig. 11. The title of each subgraph indicates the pore size range being examined. The x-axis represents the PV characterized by LTNA, while the y-axis represents the PV characterized by LAM-SEM. The black line represents the 45° line, and each point represents a sample. Points closer to the 45° line indicate a closer agreement between the results obtained by the two methods.

Among all the subgraphs, it can be observed that the PVs between 32 and 48 nm obtained by applying the CondSim method on LAM-SEM images and the Equ model on LNTA isotherms are closest. For all the

other comparisons, the LNTA inversed PVs are higher than the LAM-SEM-analysis one. There are two main reasons for this feature. Firstly, the pores with a size close to the imaging resolution cannot be fully resolved through LAM-SEM. According to the study conducted by Wu et al. [52], a portion of pores with a diameter smaller than 30 nm might not be captured with the LAM-SEM imaging method. There is a possibility that pores close to the resolution of SEM imaging may not be identified. The lower limit of this range, 20 nm, is highly consistent with the lower limit of pore diameter that can be fully captured by LAM-SEM, as indicated by previous studies [52]. The second reason lies in the inconsistency of the underlying principles between the analysis methods. The EqDia method for LAM-SEM images does not account for the variation in condensation conditions within different parts of the connected domain. Instead, it calculates the equivalent area circle diameter as a whole, resulting in PV distributions in larger size ranges. On the other hand, the Ads model for LTNA isotherms considers liquid bridge condensation within the pores, with condensation pressure lagging behind. This model tends to underestimate the pore sizes when interpreting concave meniscus condensation. For shale, the pore network effect is more prominent [53], and the condensation hysteresis phenomenon in the adsorption branch is less pronounced [44,54,55], and gas condenses through the gas–liquid two-phase meniscus. The equilibrium transition model is more suitable to describe the process. In conclusion, the use of the N_2-QSDFT-Sl/Cy-Equ model considering equilibrium transition is more appropriate.

3.4. Correlation between V_L and SSA determined by LTCA and LTNA

Previous studies have indicated a strong positive correlation between the specific surface area (SSA) obtained from LTGA characterization of shale samples and their methane adsorption capacity [21]. In this study, different LTGA methods and inversion models were employed to obtain corresponding PSDs, which can further calculate the SSAs. By conducting a correlation analysis between the SSA results obtained from different methods and the characteristic parameters of high-pressure methane adsorption, valuable insights can be gained to guide the selection of pore size analysis methods.

Fig. 12 illustrates the correlation analysis results between the Langmuir volume (V_L) obtained from high-pressure methane isothermal adsorption experiments on shale samples and the SSA obtained from LTNA with the QSDFT-Sl/Cy-Equ inversion model, as well as the SSA obtained from LTCA with the GCMC inversion model, and the combined SSA obtained by integrating the results from both methods. When integrating the LTNA and LTCA results, the PSD of the overlapping region was determined based on the results revealed by LTCA.

It can be observed that the linear fit between the combined SSA obtained from the integration of both methods and the Langmuir volume (V_L) demonstrates a higher goodness of fit compared to the fit between the SSA from LTCA and V_L. The fit between the SSA from LTNA and V_L is the lowest among the three. This indicates that the correlation between V_L and the SSA of micropores smaller than 2 nm is stronger, while there are some micro PVs that remain undetected by LTNA, resulting in a slightly lower correlation. The contribution of undetected micropores in shale to adsorption cannot be ignored. Among the 106 shale samples, the samples from the BS22 well show a significant contribution from these micropores, indicating that relying solely on LTNA characterization may not provide a comprehensive assessment. Similarly, LTCA also has limitations in detecting SSAs of certain mesopores. Overall, the combination of LTNA and LTCA provides a more comprehensive characterization of PSD within a wider range, making it a preferable choice.

The 106 shale samples studied were collected from various sublayers or formations and different shale gas wells within the research area. The strong correlation between the SSA and the V_L indicates that, for the shale within the region, the SA of the pores is one of the key factors influencing the methane adsorption capacity.

4. Conclusion

This study addresses the insufficient basis for inversion model selection for LTGA methods and the unclear correlation between their result and large-area mosaic scanning electron microscopy analysis results when characterizing complex pore structures and a wide range of PSD in shale. The research was conducted on shale samples from the Wufeng and Longmaxi Formation in the southern Sichuan Basin, China. Analysis was conducted on 106 shale samples from different wells and sublayers or formations, resulting in selection criteria that are more statistically significant and universally applicable. The main characteristics and conclusion of this study are as follows:

1) The recommended inversion models for CO_2 and N_2 adsorption, which are CO_2-GCMC and QSDFT-Sl/Cy-Equ, were optimized based on their respective fitting errors, correlation between them, and correlation between LAM-SEM and LTNA. This optimization process ensured a more comprehensive and thorough basis for selection.
2) The study demonstrated that the pore volume (PV) characterized by LAM-SEM in the 32–48 nm range, as well as the PV characterized by LTNA, showed good consistency. This suggests that the percentage of PV represented by LAM-SEM at the sub-micrometer level is representative. However, it should be noted that gas adsorption pore size analysis methods may include a portion of the volume of irregularly shaped pores with larger sizes into the smaller pore size range.
3) Through the correlation analysis between LTNA SSA and high-pressure methane adsorption parameters, it was clarified that both micropores and mesopores contribute to methane adsorption and need to be comprehensively characterized.

CRediT authorship contribution statement

Wenbin Jiang: Writing – original draft, Methodology, Conceptualization. **Mian Lin:** Supervision, Funding acquisition. **Chao Luo:** Resources, Data curation. **Zhuo Chen:** Visualization. **Gaohui Cao:** Writing – review & editing, Formal analysis. **Lili Ji:** Investigation. **Wenchao Dou:** Investigation. **Kesu Zhong:** Validation. **Fang Hao:** Supervision.

Declaration of competing interest

The authors declare that they have no known competing financial interests or personal relationships that could have appeared to influence the work reported in this paper.

Data availability

Data will be made available on request.

Acknowledgment

This work is supported by the National Natural Science Foundation of China (Grant No. 42030808, 41690132, and 41406124), the Strategic Priority Research Program of the Chinese Academy of Sciences (Grant No. XDA14010304, 2020BA19), the PetroChina Science and Technology Major Project (2019F-31-01). Special thanks to Prof. Tian Hui from Guangzhou Institute of Geochemistry, Chinese Academy of Sciences for providing the environment for using Quantachrome® AsiQwin™ software.

Appendix

Representative element area (REA) analysis of pore area fraction for LAM-SEM images

Taking the BS22-1D sample as an example, the porosity (pore area

fraction) of the entire LAM-SEM images with a size of 400 μm × 400 μm is calculated. Starting with a field of view (FOV) of 10 μm × 10 μm, the FOV is gradually increased to 400 μm × 400 μm. For each FOV, sub-domains are randomly selected from the entire LAM-SEM image, and the corresponding porosity is calculated. Therefore, the range of the porosity variation with changing FOV size is depicted in Fig. A1. It can be observed that when the FOV size exceeds 200 μm, the range of porosity variation becomes narrow, indicating that at this point, the representative element area (REA) is reached.

Comparison of PSDs derived with different model from LTCA and LTNA isotherms

Three typical samples are selected from the total 106 samples for comparision. For each sample, the distributions of differential pore volume versus pore diameter derived from the LTCA isotherm with NLDFT and GCMC models and the LTNA isotherm with Sl/Cy-QSDFT-Equ model are plotted in one graph. As shown in the following figures, the CO_2-NLDFT derived PSD has a narrower peak around 0.8 nm, while the width of the peaks founded in PSD derived by CO_2-GCMC and N_2-Sl/Cy-QSDFT-Equ model are more consistent.

References

[1] J. Wu, Y. Yuan, S. Niu, X. Wei, J. Yang, Multiscale characterization of pore structure and connectivity of wufeng-longmaxi shale in Sichuan Basin, China, Marine and Petroleum Geology 120 (2020) 104514, https://doi.org/10.1016/j.marpetgeo.2020.104514.

[2] W. Jiang, M. Lin, Z. Yi, H. Li, S. Wu, Parameter determination using 3D FIB-SEM images for development of effective model of shale gas flow in nanoscale pore clusters, Transp Porous Med 117 (2017) 5–25, https://doi.org/10.1007/s11242-016-0817-5.

[3] G. Cao, M. Lin, L. Ji, W. Jiang, M. Yang, Characterization of pore structures and gas transport characteristics of longmaxi shale, Fuel 258 (2019) 116146, https://doi.org/10.1016/j.fuel.2019.116146.

[4] C. Zou, D. Dong, Y. Wang, X. Li, J. Huang, S. Wang, Q. Guan, C. Zhang, H. Wang, H. Liu, W. Bai, F. Liang, W. Lin, Q. Zhao, D. Liu, Z. Yang, P. Liang, S. Sun, Z. Qiu, Shale gas in China: characteristics, challenges and prospects (I), Petroleum Exploration and Development 42 (2015) 753–767, https://doi.org/10.1016/S1876-3804(15)30072-0.

[5] X. Ma, J. Xie, R. Yong, Y. Zhu, Geological characteristics and high production control factors of shale gas reservoirs in silurian longmaxi formation, southern Sichuan Basin, SW China, Petroleum Exploration and Development 47 (2020) 901–915, https://doi.org/10.1016/S1876-3804(20)60105-7.

[6] R.G. Loucks, R.M. Reed, Scanning-electron-microscope petrographic evidence for distinguishing organic-matter pores associated with depositional organic matter versus migrated organic matter in mudrocks, GCAGS Journal 3 (2014) 51–60.

[7] Y. Wu, P. Tahmasebi, C. Lin, C. Dong, Process-based and dynamic 2D modeling of shale samples: considering the geology and pore-system evolution, International Journal of Coal Geology 218 (2020) 103368, https://doi.org/10.1016/j.coal.2019.103368.

[8] J. Xiong, Y. Li, S. Zhou, X. Liu, H. Han, L. Liang, J. Zhao, Insights into the pore structure characteristics of the lower silurian longmaxi formation shale in the jiaoshiba area Southern Sichuan Basin, China, J Petrol Explor Prod Technol 12 (2022) 2857–2868, https://doi.org/10.1007/s13202-022-01486-1.

[9] L. Ji, M. Lin, W. Jiang, G. Cao, J. Zhou, C. Luo, Investigation into the apparent permeability and gas-bearing property in typical organic pores in shale rocks, Marine and Petroleum Geology 110 (2019) 871–885, https://doi.org/10.1016/j.marpetgeo.2019.08.030.

[10] K. Zhang, S. Jiang, R. Zhao, P. Wang, C. Jia, Y. Song, Connectivity of organic matter pores in the lower silurian longmaxi formation shale, Sichuan Basin, southern China: analyses from helium ion microscope and focused ion beam scanning electron microscope, Geological Journal 57 (2022) 1912–1924, https://doi.org/10.1002/gj.4387.

[11] H. Tian, L. Pan, T. Zhang, X. Xiao, Z. Meng, B. Huang, Pore characterization of organic-rich lower cambrian shales in qiannan depression of Guizhou Province, southwestern China, Marine and Petroleum Geology 62 (2015) 28–43, https://doi.org/10.1016/j.marpetgeo.2015.01.004.

[12] S. Fu, Q. Fang, A. Li, Z. Li, J. Han, X. Dang, W. Han, Accurate characterization of full pore size distribution of tight sandstones by low-temperature nitrogen gas adsorption and high-pressure mercury intrusion combination method, Energy Science & Engineering 9 (2021) 80–100, https://doi.org/10.1002/ese3.817.

[13] J. Zhao, Z. Jin, Q. Hu, Z. Jin, T.J. Barber, Y. Zhang, M. Bleuel, Integrating SANS and fluid-invasion methods to characterize pore structure of typical american shale oil reservoirs, Sci. Rep. 7 (2017) 15413, https://doi.org/10.1038/s41598-017-15362-0.

[14] Y. Qian, P. Gao, X. Fang, F. Sun, Y. Cai, Y. Zhou, Microstructure characterization techniques for shale reservoirs: a review, Front. Earth Sci. 10 (2022) 930474, https://doi.org/10.3389/feart.2022.930474.

[15] L. Leu, A. Georgiadis, M.J. Blunt, A. Busch, P. Bertier, K. Schweinar, M. Liebi, A. Menzel, H. Ott, Multiscale description of shale pore systems by scanning SAXS and WAXS microscopy, Energy Fuels 30 (2016) 10282–10297, https://doi.org/10.1021/acs.energyfuels.6b02256.

[16] B.X. Medina-Rodriguez, V. Alvarado, Use of gas adsorption and inversion methods for shale pore structure characterization, Energies 14 (2021) 2880, https://doi.org/10.3390/en14102880.

[17] Y. Cai, Q. Li, D. Liu, Y. Zhou, D. Lv, Insights into matrix compressibility of coals by mercury intrusion porosimetry and N2 adsorption, International Journal of Coal Geology 200 (2018) 199–212, https://doi.org/10.1016/j.coal.2018.11.007.

[18] M.M. Labani, R. Rezaee, A. Saeedi, A.A. Hinai, Evaluation of pore size spectrum of gas shale reservoirs using low pressure nitrogen adsorption, gas expansion and mercury porosimetry: a case study from the Perth and canning basins, Western Australia, Journal of Petroleum Science and Engineering 112 (2013) 7–16, https://doi.org/10.1016/j.petrol.2013.11.022.

[19] P. Bertier, K. Schweinar, H. Stanjek, A. Ghanizadeh, C.R. Clarkson, A. Busch, N. Kampman, D. Prinz, A. Amann-Hildebrand, B.M. Krooss, V. Pipich, On the use and abuse of N2 physisorption for the characterization of the pore structure of shales, in: pp. 151–161.

[20] H. He, P. Liu, L. Xu, S. Hao, X. Qiu, C. Shan, Y. Zhou, Pore structure representations based on nitrogen adsorption experiments and an FHH fractal model: case study of the block Z shales in the Ordos Basin, China, Journal of Petroleum Science and Engineering 203 (2021) 108661, https://doi.org/10.1016/j.petrol.2021.108661.

[21] Y. Wang, Y. Zhu, S. Liu, R. Zhang, Pore characterization and its impact on methane adsorption capacity for organic-rich marine shales, Fuel 181 (2016) 227–237, https://doi.org/10.1016/j.fuel.2016.04.082.

[22] H. Mi, Y. Guo, X. Yu, Study on pore structure of shale reservoir by low temperature nitrogen adsorption method, Geofluids 2022 (2022) 1–10, https://doi.org/10.1155/2022/9355020.

[23] B. Zhang, Y. Chen, Particle size effect on pore structure characteristics of lignite determined via low-temperature nitrogen adsorption, Journal of Natural Gas Science and Engineering 84 (2020) 103633, https://doi.org/10.1016/j.jngse.2020.103633.

[24] H. Han, P. Pang, N. Zhong, Q. Luo, Y. Ma, Y. Gao, The pore characteristics and gas potential of the jurassic continental shales in the middle-small basins, Northwest China, Journal of Petroleum Science and Engineering 188 (2020) 106873, https://doi.org/10.1016/j.petrol.2019.106873.

[25] P.I. Ravikovitch, A. Vishnyakov, A.V. Neimark, Density functional theories and molecular simulations of adsorption and phase transitions in nanopores, Phys. Rev. E Stat. Nonlin. Soft Matter Phys. 64 (2001) 11602, https://doi.org/10.1103/PhysRevE.64.011602.

[26] P.I. Ravikovitch, A.V. Neimark, Characterization of micro- and mesoporosity in SBA-15 materials from adsorption data by the NLDFT method, J. Phys. Chem. B 105 (2001) 6817–6823, https://doi.org/10.1021/jp010621u.

[27] M.-L. Han, X.-L. Wei, J.-C. Zhang, Y. Liu, X. Tang, P. Li, Z.-Y. Liu, Influence of structural damage on evaluation of microscopic pore structure in marine continental transitional shale of the southern North China Basin: a method based on the low-temperature N2 adsorption experiment, Petroleum Science 19 (2022) 100–115, https://doi.org/10.1016/j.petsci.2021.10.016.

[28] J. Xiong, X. Liu, L. Liang, Experimental study on the pore structure characteristics of the upper ordovician wufeng formation shale in the southwest portion of the Sichuan Basin, China, Journal of Natural Gas Science and Engineering 22 (2015) 530–539, https://doi.org/10.1016/j.jngse.2015.01.004.

[29] H. Zhan, X. Li, Z. Hu, X. Duan, W. Guo, Y. Li, Influence of particle size on the low-temperature nitrogen adsorption of deep shale in southern Sichuan, China, Minerals 12 (2022) 302, https://doi.org/10.3390/min12030302.

[30] Y. Chen, L. Wei, M. Mastalerz, A. Schimmelmann, The effect of analytical particle size on gas adsorption porosimetry of shale, International Journal of Coal Geology 138 (2015) 103–112, https://doi.org/10.1016/j.coal.2014.12.012.

[31] Y. Wang, H. Cheng, Q. Hu, L. Liu, L. Jia, S. Gao, Y. Wang, Pore structure heterogeneity of wufeng-longmaxi shale, Sichuan Basin, China: evidence from gas physisorption and multifractal geometries, Journal of Petroleum Science and Engineering 208 (2022) 109313, https://doi.org/10.1016/j.petrol.2021.109313.

[32] L. Qi, X. Tang, Z. Wang, X. Peng, Pore characterization of different types of coal from coal and gas outburst disaster sites using low temperature nitrogen adsorption approach, international journal of, Mining Science and Technology 27 (2017) 371–377, https://doi.org/10.1016/j.ijmst.2017.01.005.

[33] G. Wang, Y. Ju, Organic shale micropore and mesopore structure characterization by ultra-low pressure N 2 physisorption: experimental procedure and interpretation model, Journal of Natural Gas Science and Engineering 27 (2015) 452–465, https://doi.org/10.1016/j.jngse.2015.08.003.

[34] H. Sharifigaliuk, S.M. Mahmood, R. Rezaee, F. Ayobami Afolabi, I., Ul haq, shale's pore structure and sorption-diffusion characteristics: effect of analyzing methods and particle size, Energy Fuels 36 (2022) 6167–6186, https://doi.org/10.1021/acs.energyfuels.2c00850.

[35] L. Zhang, Y. Xiong, Y. Li, M. Wei, W. Jiang, R. Lei, Z. Wu, DFT modeling of CO 2 and ar low-pressure adsorption for accurate nanopore structure characterization in organic-rich shales, Fuel 204 (2017) 1–11, https://doi.org/10.1016/j.fuel.2017.05.046.

[36] J. Li, J. Yin, Y. Zhang, S. Lu, W. Wang, J. Li, F. Chen, Y. Meng, A comparison of experimental methods for describing shale pore features — a case study in the Bohai Bay basin of eastern China, International Journal of Coal Geology 152 (2015) 39–49, https://doi.org/10.1016/j.coal.2015.10.009.

[37] P. Pang, H. Han, L. Hu, C. Guo, Y. Gao, Y. Xie, The calculations of pore structure parameters from gas adsorption experiments of shales: which models are better?

Journal of Natural Gas Science and Engineering 94 (2021) 104060 https://doi.org/10.1016/j.jngse.2021.104060.
[38] M. Wang, Z. Li, Z. Liang, Z. Jiang, W. Wu, Method selection for analyzing the mesopore structure of shale—Using a combination of multifractal theory and low-pressure gas adsorption, Energies 16 (2023) 2464, https://doi.org/10.3390/en16052464.
[39] M. Wei, L. Zhang, Y. Xiong, J. Li, P. Peng, Nanopore structure characterization for organic-rich shale using the non-local-density functional theory by a combination of N2 and CO2 adsorption, Microporous and Mesoporous Materials 227 (2016) 88–94, https://doi.org/10.1016/j.micromeso.2016.02.050.
[40] W. Jiang, G. Cao, C. Luo, M. Lin, L. Ji, J. Zhou, A composition-based model for methane adsorption of overmature shales in wufeng and longmaxi formation, Sichuan Basin, Chemical Engineering Journal 429 (2022) 130766, https://doi.org/10.1016/j.cej.2021.130766.
[41] D.P. Singh, D. Chandra, V. Vishal, B. Hazra, P. Sarkar, Impact of degassing time and temperature on the estimation of pore attributes in shale, Energy Fuels 35 (2021) 15628–15641, https://doi.org/10.1021/acs.energyfuels.1c02201.
[42] Y. Yuan, R. Rezaee, M. Verrall, S.-Y. Hu, J. Zou, N. Testmanti, Pore characterization and clay bound water assessment in shale with a combination of NMR and low-pressure nitrogen gas adsorption, International Journal of Coal Geology 194 (2018) 11–21, https://doi.org/10.1016/j.coal.2018.05.003.
[43] R. Shen, X. Zhang, H. Yang, H. Ren, H. Guo, H. Zhou, Micropore structure and fractal characteristics of shale in Midwest China, J Petrol Explor Prod Technol (2024), https://doi.org/10.1007/s13202-024-01747-1.
[44] W. Lai, S. Yang, Y. Jiang, F. Zhao, Z. Li, B. Zaman, M. Fayaz, X. Li, Y. Chen, Artefact peaks of pore size distributions caused by unclosed sorption isotherm and tensile strength effect, Adsorption 26 (2020) 633–644, https://doi.org/10.1007/s10450-020-00228-1.
[45] R. Holmes, E.C. Rupp, V. Vishal, J. Wilcox, Selection of shale preparation protocol and outgas procedures for applications in low-pressure analysis, Energy Fuels 31 (2017) 9043–9051, https://doi.org/10.1021/acs.energyfuels.7b01297.
[46] F.J. Medina, I. Jausoro, M.A. Floridia Addato, M.J. Rodriguez, F.G. Tomassini, A. Caneiro, On the evaluation of representative elementary area for porosity in shale rocks by field emission scanning electron microscopy, Energy 253 (2022) 124141, https://doi.org/10.1016/j.energy.2022.124141.
[47] P. Psarras, R. Holmes, V. Vishal, J. Wilcox, Methane and CO2 adsorption capacities of kerogen in the eagle ford shale from molecular simulation, Acc. Chem. Res. 50 (2017) 1818–1828, https://doi.org/10.1021/acs.accounts.7b00003.
[48] D. Chandra, V. Vishal, A. Debbarma, S. Banerjee, S.P. Pradhan, M.K. Mishra, Role of composition and depth on pore attributes of Barakar formation gas shales of Ib Valley, India, using a combination of low-pressure sorption and image analysis, Energy Fuels 34 (2020) 8085–8098, https://doi.org/10.1021/acs.energyfuels.0c00746.
[49] M. Thommes, Pore size analysis by gas adsorption. part I: aspects of the application of density functional theory (DFT) and Monte Carlo simulation (MC) for micro/mesopore size analysis, Quantachrome Instrum. Powder Tech. Note 31 (2002).
[50] J.L. Rodgers, W.A. Nicewander, Thirteen ways to look at the correlation coefficient, The American Statistician 42 (1998) 59–66.
[51] D. Schneider, R. Valiullin, Capillary condensation and evaporation in irregular channels: sorption isotherm for serially connected pore model, J. Phys. Chem. C 123 (2019) 16239–16249, https://doi.org/10.1021/acs.jpcc.9b03626.
[52] J. Wu, C. Luo, K. Zhong, Y. Li, G. Li, Z. Du, J. Yang, Innovative characterization of organic nanopores in marine shale by the integration of HIM and SEM, Energy 282 (2023) 128390, https://doi.org/10.1016/j.energy.2023.128390.
[53] Z. Chen, M. Lin, W. Jiang, G. Cao, Molecular simulation of nitrogen adsorption in multidimensional nanopores and new insights into the inversion of pore size distribution for gas shale, Energies 16 (2023) 8066, https://doi.org/10.3390/en16248066.
[54] Y. Zeng, C. Fan, D.D. Do, D. Nicholson, Evaporation from an ink-bottle pore: mechanisms of adsorption and desorption, Ind. Eng. Chem. Res. 53 (2014) 15467–15474, https://doi.org/10.1021/ie500215x.
[55] P.T.M. Nguyen, D.D. Do, D. Nicholson, On the hysteresis loop of argon adsorption in cylindrical pores, J. Phys. Chem. C 115 (2011) 4706–4720, https://doi.org/10.1021/jp111254j.